

Morphology Control of Tantalum Carbide Nanoparticles through Dopant Additions

Tianqi Ren,[#] Richard Tran,[#] Sebastian Lee, Aric Bandera, Manuel Herrera, Xiang-Guo Li, Shyue Ping Ong,^{*} and Olivia A. Graeve^{*}

Cite This: *J. Phys. Chem. C* 2021, 125, 10665–10675

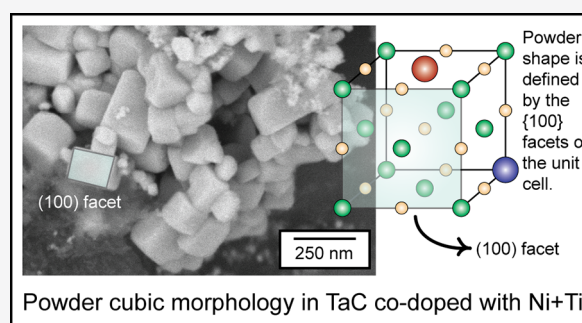
Read Online

ACCESS |

Metrics & More

Article Recommendations

ABSTRACT: The control of powder morphology in metals and ceramics is of critical importance in applications such as catalysis and chemical sensing whereby specific crystal facets better facilitate chemical reactions. In response to this challenge, we present a combined experimental and computational approach that examines the principles behind dopant-induced crystallographic faceting in nanoparticles. We base our study on nanoparticles of tantalum carbide doped with nickel, iron, cobalt, niobium, and titanium and observe a very significant transition from round/irregular particle shapes to cubes and cuboctahedrons upon the addition of transition metal dopants. The presence of the dopants, which segregate toward the surface of the particles, results in atomic orbital hybridization, causing a significant decrease of up to $0.13 \text{ eV}\cdot\text{\AA}^{-2}$ in the surface energy of the (100) facets, thus providing the driving force for the formation of nanocubes with exposed (100) surfaces. These principles can be generalized to other ceramics and serve as guidance for the optimized control of shape in powders. For example, if one seeks to produce highly faceted V-, Hf-, or Zr-carbide nanoparticles, doping strategies reported here can be applied. Other elements may also be effective in changing the growth habits of crystals based on surface segregation and dopant–host atomic orbital hybridization.



Powder cubic morphology in TaC co-doped with Ni+Ti

INTRODUCTION

Tantalum carbide (TaC) is an ultrahigh-temperature ceramic (UHTC) with a melting temperature of $\sim 4100 \text{ K}$ and exceptional hardness, attributed to its strong Ta–C covalent bonds.^{1,2} Such properties hold great engineering relevance under harsh conditions, resulting in industrial applications such as high-speed cutting tools and hard coatings. TaC also holds great potential in aerospace and advanced energy systems, such as turbine blades, scramjet engines, nuclear reactors, and solar absorbers.³ Practical limitations of TaC at high temperatures are often due to the degradation of mechanical properties due to porosity and other microstructural defects, as well as problems connected to oxidation⁴ and creep deformation.⁵

The improvement of properties begins with the control of powder size and shape. Studies have explored the shape control of transition metal carbide nanoparticles to exploit the high surface area-to-volume ratio in applications such as gas adsorption⁶ and chemical sensing whereby specific facets, such as those with steps and kinks, will better facilitate chemical reactions.^{7,8} Modeling studies have looked at the molecular adsorption of H_2O on ZrC , to obtain cubes and octahedrons, and carbon adsorption on Ru to produce nanorods.⁹ Strain effects have also been explored as parameters for morphological modification of copper and nickel

particles,¹⁰ and doping has been applied for obtaining nanorods of magnesium.¹¹ In addition, modeling^{12–17} and experimental techniques^{18–23} have been applied for exploring the behavior of borides of cubic and other morphologies. Moreover, experimental efforts have investigated shape change in cubic carbides as a function of carbon stoichiometry, which influences the relative growth rate of the dominant {111} and {100} facets.^{24–26}

Recently, doping has been suggested as a possible mechanism to form nanocubes in ceramic materials. For transition metal dopants, the interactions between the *d* orbitals of dopants and the *p* orbitals of the nonmetallic anionic elements (i.e., carbon, nitrogen, boron, etc.) in ceramic compounds are thought to promote adsorption on the {100} facets, especially for metallic dopants with high carbon solubility.^{24,27} With this in mind, the modification of particles from octahedrons to cuboids with an increasing dopant

Received: February 15, 2021

Revised: April 29, 2021

Published: May 7, 2021



concentration has been successfully demonstrated for Cr-doped WO_3 and Ni-doped TiC.^{8,24} However, the fundamental principles behind dopant-induced morphological selectivity and control remain largely unknown.

In this study, a combined experimental and computational effort is implemented to demonstrate the effects of dopants on the particle morphology of TaC. We show that morphology modification results from a combination of dopant segregation toward the surface of particles and dopant interaction with surface carbon through orbital hybridization. These effects modify surface energy, slowing crystal growth and facilitating the formation of polyhedrons. Doping with iron and co-doping with nickeltitanium results in cubes and cuboctahedrons, whereas cobalt and nickel doping results in cuboctahedrons. This work provides critical insights into the fundamentals of dopant-induced shape control, which has exceptional potential in tuning the mechanical and catalytic properties of ceramic materials.

■ EXPERIMENTAL METHODS

Synthesis of Powders. The synthesis of TaC particles is based on a modified solvothermal method.^{28,29} Tantalum(V) chloride (No. 14614, 99.8%, anhydrate, Sigma-Aldrich) and carbon black powder (No. 39724, >99.9%, Alfa Aesar) were used as the metal and carbon sources. Lithium granules (No. 499811, 99%, Sigma-Aldrich) were employed as the non-aqueous solvent and reductant, according to a $\text{TaCl}_5 + \text{C} + 5\text{Li} \rightarrow \text{TaC} + 5\text{LiCl}$ chemistry. The amount of each component was calculated based on a 3 g theoretical yield of TaC, while two times of excess carbon and lithium were used to ensure the formation of TaC without intermediate phases. For the incorporation of dopants, metallic nickel (No. A17943, 99.9% metals basis, Alfa Aesar), iron (No. 267953, >99.9% metals basis, Sigma-Aldrich), cobalt (No. 697745, >99.9% metals basis, Sigma-Aldrich), titanium (No. 43102, 99.5% metals basis, Alfa Aesar), and niobium (No. 11548, 99.9% metals basis, Alfa Aesar) were used during synthesis. Their amounts varied based on various atomic ratios between the dopant and the host. To lower the maximum flame temperature, 30 wt % of pure TaC powders (No. 12144, 99.5%, Alfa Aesar) was added as the reaction diluent. The precursors were weighed and ground manually in a mortar and pestle in an argon-protected glovebox for at least 15 min to create a homogeneous mixture. They were then placed in a quartz test tube, after which lithium granules were incorporated. The test tube was then rotated repeatedly to ensure that the surfaces of the lithium granules were fully covered with precursor powders and temporarily sealed with parafilm for transfer out of the glovebox. To minimize oxidation, the test tube was then capped by a rubber stopper, flushed with ultrahigh-purity argon gas five times, and connected to a vacuum pump for outgassing. To initialize the reaction, a volumetric external heating apparatus was custom-made using a stainless steel hollow cylinder wrapped with dual-element high-temperature heating tape. The system was preheated to ~ 673 K in order for the reaction to occur. After flushing, the test tube was inserted into the heating cylinder, and the reaction self-ignited once the system reached the melting temperature of lithium. The duration of the reaction was less than 40 s for all experiments. The system was then air-cooled to room temperature. The post-reaction products were rinsed using deionized water to dissolve excess lithium, followed by two wash cycles using hydrochloric acid (H-135, 25 vol %,

Spectrum Chemical). Within each cycle, 15 min of magnetic stirring and 30 min of ultrasonication were applied for thoroughness of washing and deagglomeration. Finally, the acid-washed powders were cleaned one more time using deionized water and rinsed with ethanol. The resulting powders were collected after 24 h of drying in air.

Characterization. The phase purity of the powder samples was analyzed by X-ray diffraction on a D2 Phaser (Bruker AXS, Inc., Madison, WI) using $\text{CuK}\alpha$ radiation. The morphologies of the particles were imaged using scanning electron microscopy (SEM) on an Apreo instrument (ThermoFisher Scientific, Hillsboro, OR). Elemental composition was analyzed using energy dispersive spectroscopy (EDS) on the SEM and by X-ray photoelectron spectroscopy (XPS) on a custom-designed system (SPECS Surface Nano Analysis GmbH, Berlin, Germany) equipped with a PHOIBOS 150 WAL analyzer with a DDL-2 detector and a FOCUS 500/600 ellipsoidal monochromatic X-ray source with a dual anode of Al and Ag. EDS and XPS were employed for the determination of bulk and surface chemical composition, respectively. The elemental surface compositions were calculated by deconvolution of individual peaks using CasaXPS software. To statistically determine the morphological modifications, particles were evaluated based on multiple SEM images. At least 900 particles were counted for each sample, ensuring the randomness and statistical significance of the sampling. For each dopant precursor concentration, two individual batches of powders were synthesized and characterized using identical procedures to confirm the repeatability of the results.

■ COMPUTATIONAL METHODS

General. All DFT calculations were performed using the Vienna Ab initio Simulation Package (VASP) within the projector augmented wave (PAW) approach.^{30–33} The pseudopotentials used were similar to those used in the Materials Project.³⁴ The PAW potential describes the core electrons with the frozen core approximation, while the valence electron configurations of tantalum, carbon, titanium, iron, cobalt, nickel, and niobium are given by Ta: $5p^6 6s^2 5d^3$, C: $2s^2 2p^2$, Ti: $3p^6 3d^3 4s^1$, Fe: $3p^6 3d^7 4s^1$, Co: $3d^8 4s^1$, Ni: $3p^6 3d^9 4s^1$, and Nb: $4p^6 5s^2 4d^3$. The exchange–correlation effects were modeled using the Perdew–Burke–Ernzerhof (PBE) generalized gradient approximation (GGA) functional, and all calculations were spin-polarized with a plane wave cutoff of 400 eV.³⁵ The energies and atomic forces of all calculations were converged within 1×10^{-4} eV and 0.02 eV·Å⁻¹, respectively. Γ -centered k -point meshes of $\frac{50}{a} \times \frac{50}{b} \times \frac{50}{c}$ and $\frac{50}{a} \times \frac{50}{b} \times 1$ were used for bulk and slab calculations, respectively, with noninteger values rounded up to the nearest integer.³⁶ Both the volume and atomic positions were relaxed for all undoped bulk systems, while only the atomic positions of the slabs and doped systems were relaxed. Since there are several possible terminations for the TaC(111) facet, we only investigated segregation in the most stable terminations. Furthermore, after the surface energy (γ) was determined for several facets, it was used to construct the Wulff shape. Further explanation and details of the surface grand potential can be found in the next section.

By comparing dopant stability in the surface and bulk, defined as the energy difference between a doped and an undoped cell, we determined where the dopant segregates. This is dictated by the segregation energy, which is given by

Table 1. Coefficients and Constants (See Eq 15) Used to Calculate the Surface Energy as a Function of $\Delta\mu_i$ for All Slab Models^a

	(hkl)	dopant (X)	site	Γ_C	Γ_X	Γ_{Ti}	$\gamma(\Delta\mu_i = 0)$
1	(100)	undoped	–	–	–	–	0.0915
2	(111)	undoped	–	0.0576	–	–	0.1849
3	(100)	Ni	sub	–0.0199	–0.0199	–	0.0328
4	(111)	Ni	surf	0.0346	–0.0230	–	0.0648
5	(100)	Co	sub	–0.0199	–0.0199	–	0.0251
6	(111)	Co	surf	0.0346	–0.0230	–	0.0563
7	(100)	Fe	sub	–0.0199	–0.0199	–	0.0240
8	(111)	Fe	surf	0.0346	–0.0230	–	0.0614
9	(100)	Nb	sub	–0.0199	–0.0199	–	–0.0662
10	(111)	Nb	surf	0.0346	–0.0230	–	–0.0035
11*	(100)	undoped	–	0.0169	–	0.0169	0.1206
12*	(111)	undoped	–	0.0584	–	–	0.1960
13*	(100)	Ni	sub	–0.0169	–0.0253	0.0084	0.0415
14*	(111)	Ni	surf	0.0195	–0.0292	–0.0097	0.0141

^aValues of Γ_i are the coefficients of $\Delta\mu_i$ in units of \AA^{-2} and represent the coverages of species i at the surface, while the units of the constant $\gamma(\Delta\mu_i = 0)$ are $\text{eV}\cdot\text{\AA}^{-2}$. Entries labeled with * correspond to values for TiTa_3C_4 .

$$E_{\text{seg}} = \frac{(E^{\text{slab}+X} - E^{\text{slab}})}{2} - (E^{\text{bulk}+X} - E^{\text{bulk}}) \quad (1)$$

The difference between $E^{\text{slab}+X}$ and E^{slab} , the calculated total energies of the doped and undoped slab cells, respectively, represents the dopant stability on the surface. Meanwhile, the difference between $E^{\text{bulk}+X}$ and E^{bulk} , the calculated total energies of the doped and undoped bulk supercells, respectively, represents the dopant stability in the bulk. The factor of 2 in the first term accounts for both surfaces being symmetrically doped. $E_{\text{seg}} < 0$ indicates a segregation tendency toward the surface, $E_{\text{seg}} \sim 0$ indicates no segregation tendency, and $E_{\text{seg}} > 0$ indicates a segregation tendency toward the bulk. Only dopants that segregate toward the surface are assumed to influence the surface energy and thus affect the morphology. Thus, we investigated dopant segregation in both the top layer and sublayer of the surface.

All rocksalt ($Fm\bar{3}m$) TaC slabs and bulk supercells were constructed from its conventional unit cell with a relaxed lattice parameter of 4.48 \AA , which is consistent with the experimental value of 4.45 \AA .³⁷ We also investigated slabs of TiTa_3C_4 as a computational analogue to solid solutions of TaC with Ti dopant. TiTa_3C_4 slabs were generated from a fully relaxed bulk TiTa_3C_4 structure with a lattice parameter of 4.45 \AA , which was in turn generated by substituting one Ta atom for Ti in the conventional unit cell of TaC. Dopant substitution of a single Ta atom was performed for both TaC slabs and bulk supercells. We investigated the most dilute coverage of dopants that can be calculated while maintaining slab systems of less than 200 atoms resulting in a coverage of 1/4 and 1/2 monolayers (number of dopants per unit primitive slab) for the TaC and TiTa_3C_4 slabs, respectively. All slabs had a slab and vacuum layer 22 and 16 \AA thick to prevent periodic interactions between the dopants and the two surfaces. The (111) and (100) slabs of TaC contained 115 and 120 atoms, respectively, while the (111) and (100) slabs of TiTa_3C_4 contained 92 and 88 atoms, respectively. The bulk supercells of TaC and TiTa_3C_4 contained 180 and 144 atoms, respectively, and shared the same lattice parameters as the corresponding slab cells used to calculate E_{seg} . The lattice parameters and number of atoms in the doped and undoped supercells were kept consistent. All slab systems, including doped slabs,

maintained symmetrically equivalent surfaces by ensuring Laue point group symmetry in the structures to avoid any dipole moments perpendicular to the surface.^{36,38,39} All computational parameters, structural models, Wulff construction, chemical potential range maps, and surface energy analysis were obtained with the aid of the Python Materials Genomics (pymatgen) materials analysis library.⁴⁰

For each dopant–carbon bond, we quantified p – d hybridization as the negative of the integrated Crystal Orbital Hamiltonian Population (–ICOHP) from the valence band to the Fermi level, which corresponds to the covalent bond contribution of the dopant. Similarly, –ICOHP was used to quantify the metallic bond contributions for each dopant–Ta bond. We only considered bonds within a radius of 3.5 \AA from the dopant, which encompasses all carbon nearest neighbors and Ta next-nearest neighbors. The –ICOHP was normalized by the number of valence electrons and the sum of the metallic (dopant–Ta) and covalent (dopant–C) contributions, which results in the total bond contribution of the dopant. We normalized –ICOHP for the covalent contributions by this total to obtain the percentage covalent contribution of the dopant. For further details, the reader is referred to Maintz et al.⁴¹ and Sun et al.⁴²

Surface Grand Potential. In general, the surface energies of TaC can be obtained from the following expression:

$$\gamma(\mu_i) = \frac{1}{2A} \left[E^{\text{slab}} - \sum_i N_i \mu_i \right] \quad (2)$$

where N_i is the number of i atoms in the slab, A is the cross-sectional area, and E^{slab} is the total DFT energy of the slab. All coefficients and constants for the surface energy provided in Table 1 can be derived from this expression. Here the chemical potential accounts for excess or deficient atomic species exchanged between the surface and an external reservoir (i.e., the surrounding environment in the form of a gas, liquid, or bulk phase). Assuming the surface phase is in equilibrium with the bulk, the chemical potentials for all species in the undoped system are connected via Gibbs free energy by

$$g_{\text{TaC}}^{\text{bulk}} = \sum_i n_i \mu_i = \mu_{\text{Ta}} + \mu_{\text{C}} \quad (3)$$

where n_i is the stoichiometry of species i per formula unit ($\eta_{\text{Ta}} = \eta_{\text{C}} = 1$ in TaC). Assuming there is no configurational entropy or pressure–volume effects, g^{bulk} can be calculated as the total bulk DFT energy per formula unit. For a stoichiometric slab of TaC, such as the undoped (100) slab of TaC (Table 1: row 1), we can substitute eq 3 into eq 2 to obtain the following expression:

$$\gamma = \frac{1}{2A} [E^{\text{slab}} - N_{\text{Ta}} g_{\text{TaC}}^{\text{bulk}}] \quad (4)$$

To account for the excess or deficiency of C in nonstoichiometric slabs, we first expand eq 2 to

$$\gamma = \frac{1}{2A} [E^{\text{slab}} - N_{\text{Ta}} \mu_{\text{Ta}} - N_{\text{C}} \mu_{\text{C}}] \quad (5)$$

We can simplify eq 5 as a function of μ_{C} by substituting eq 3 for μ_{Ta} to obtain

$$\gamma = \frac{1}{2A} [E^{\text{slab}} - N_{\text{Ta}} (g_{\text{TaC}}^{\text{bulk}} - \mu_{\text{C}}) - N_{\text{C}} \mu_{\text{C}}] \quad (6)$$

Next we must define the upper and lower bounds needed for μ_{C} to allow a reasonable range for the surface energy due to the exchange of C atoms between the surface and the external reservoir. The upper bound is set by the assumption that an excess amount of C at the surface will eventually lead to the formation of surface graphite, while the lower bound is set by the assumption that a surface deficiency of C (or equivalently an excess of Ta) will lead to the formation of Ta_2C . This range for μ_{C} is expressed as

$$E_{\text{Ta}_2\text{C}} - 2E_{\text{Ta}}^{\text{bcc}} - E_{\text{C}}^{\text{graphite}} \leq \mu_{\text{C}} \leq E_{\text{C}}^{\text{graphite}} \quad (7)$$

where $E_{\text{Ta}_2\text{C}}$ is the energy per formula unit of Ta_2C , and $E_{\text{Ta}}^{\text{bcc}}$ and $E_{\text{C}}^{\text{graphite}}$ are the energies per atom of body-centered Ta and graphite, respectively. For convenience, we set the upper bound as a zero reference by subtracting $E_{\text{C}}^{\text{graphite}}$ from μ_{C} , leaving

$$\Delta G_{\text{Ta}_2\text{C}}^{\text{f}} \leq \Delta \mu_{\text{C}} \leq 0 \quad (8)$$

where $\Delta G_{\text{Ta}_2\text{C}}^{\text{f}} = E_{\text{Ta}_2\text{C}} = 2E_{\text{Ta}}^{\text{bcc}} - E_{\text{C}}^{\text{graphite}}$ is the formation energy of Ta_2C and $\mu_{\text{C}} = \Delta \mu_{\text{C}} + E_{\text{C}}^{\text{graphite}}$. We substitute our expression for μ_{C} into eq 6 to obtain the following expression:

$$\gamma(\Delta \mu_{\text{C}}) = \frac{E^{\text{slab}} - N_{\text{Ta}} g_{\text{TaC}}^{\text{bulk}}}{2A} + \Gamma_{\text{C}}(\Delta \mu_{\text{C}} + E_{\text{C}}^{\text{graphite}}) \quad (9)$$

Here γ is now a function of the carbon chemical potential, $\Delta \mu_{\text{C}}$, relative to the energy of graphite per atom ($E_{\text{C}}^{\text{graphite}}$), and $\Gamma_{\text{C}} = \frac{1}{2A}(N_{\text{Ta}} - N_{\text{C}})$ is the number of excess or deficient C atoms per surface area (coverage), which is negative for excess C and positive for deficient C. We can obtain the surface energy of an undoped, nonstoichiometric slab (Table 1: row 2) using eq 9. In practice, $\Delta \mu_{\text{C}}$ is a function of the finite temperature and pressure of an ideal gas interacting with the surface at equilibrium. As the temperature increases, $\Delta \mu_{\text{C}}$ decreases and the formation of a surface carbon layer becomes less stable as more carbon atoms dissociate off the surface into a gas phase. Meanwhile, the pressure of the gas increases with $\Delta \mu_{\text{C}}$ resulting in the reverse effect. The relationship between $\Delta \mu_{\text{C}}$ and these external conditions is given by

$$\Delta \mu_{\text{C}}(T, P) = g(H, T, S) + k_{\text{B}} T \ln \left(\frac{P}{P_0} \right) \quad (10)$$

where k_{B} is the Boltzmann constant, $P_0 = 0.1$ MPa, and $g(H, T, S)$ is the Gibbs free energy of the carbon reference, which can be derived from thermochemical tables.⁴³

With the addition of an external component (e.g., a dopant), a new chemical potential term (μ_{X}) is added to eq 9. As with μ_{C} , we need an appropriate upper bound, which we set as $E_{\text{X}}^{\text{atom}}$, the total energy of an atom X isolated in a vacuum. We choose this reference assuming the dopant atoms will interact similarly to a metallic gas with the surface. We substitute μ_{X} into eq 9 in a manner similar to μ_{C} to yield an expression for the surface energy of a doped slab as a function of $\Delta \mu_i$ (Table 1: rows 3–10):

$$\begin{aligned} \gamma(\Delta \mu_{\text{C}}, \Delta \mu_{\text{X}}) = & \frac{E^{\text{slab}+\text{X}} - N_{\text{Ta}} g_{\text{TaC}}^{\text{bulk}}}{2A} \\ & + \Gamma_{\text{C}}(\Delta \mu_{\text{C}} + E_{\text{C}}^{\text{graphite}}) \\ & - \Gamma_{\text{X}}(\Delta \mu_{\text{X}} + E_{\text{X}}^{\text{atom}}) \end{aligned} \quad (11)$$

where $\Gamma_{\text{X}} = \frac{1}{2A} N_{\text{X}}$ is the coverage of dopant X in the slab, and $E^{\text{slab}+\text{X}}$ is the total energy of a slab with dopant X.

Similar to eq 9, for an undoped nonstoichiometric TiTa_3C_4 slab (Table 1: rows 11–12), we can solve for μ_{Ta} :

$$\mu_{\text{Ta}} = \frac{g_{\text{TiTa}_3\text{C}_4}^{\text{bulk}} - 4\mu_{\text{C}} - \mu_{\text{Ti}}}{3} \quad (12)$$

The numbers 4 and 3 in this equation correspond to the values of η_{C} and η_{Ta} , respectively. We set the upper bound of η_{Ti} as the energy per atom of a hexagonal close-packed Ti bulk system ($E_{\text{Ti}}^{\text{hcp}}$) and again rewrite eq 2 as a function of $\Delta \mu_i$:

$$\begin{aligned} \gamma(\Delta \mu_{\text{C}}, \Delta \mu_{\text{Ti}}) = & \frac{E^{\text{slab}+\text{X}} - \frac{N_{\text{Ta}}}{3} g_{\text{TiTa}_3\text{C}_4}^{\text{bulk}}}{2A} \\ & + \Gamma_{\text{C}}(\Delta \mu_{\text{C}} + E_{\text{C}}^{\text{graphite}}) - \Gamma_{\text{Ti}}(\Delta \mu_{\text{Ti}} + E_{\text{Ti}}^{\text{hcp}}) \end{aligned} \quad (13)$$

with

$$\Gamma_{\text{C}} = \frac{1}{2A} \left(\frac{4}{3} N_{\text{Ta}} - N_{\text{C}} \right)$$

and

$$\Gamma_{\text{Ti}} = \frac{1}{2A} \left(\frac{1}{3} N_{\text{Ta}} - N_{\text{Ti}} \right)$$

For a slab where only one species is nonstoichiometric, such as C in the (111) slab of TiTa_3C_4 (Table 1: row 12), eq 13 simplifies to

$$\gamma(\Delta \mu_{\text{C}}) = \frac{E^{\text{slab}+\text{X}} - \frac{N_{\text{Ta}}}{3} g_{\text{TiTa}_3\text{C}_4}^{\text{bulk}}}{2A} + \Gamma_{\text{C}}(\Delta \mu_{\text{C}} + E_{\text{C}}^{\text{graphite}}) \quad (14)$$

For a doped slab of TiTa_3C_4 (Table 1: rows 13 and 14), we again add an $N_{\text{X}} \mu_{\text{X}}$ term to eq 14 to obtain

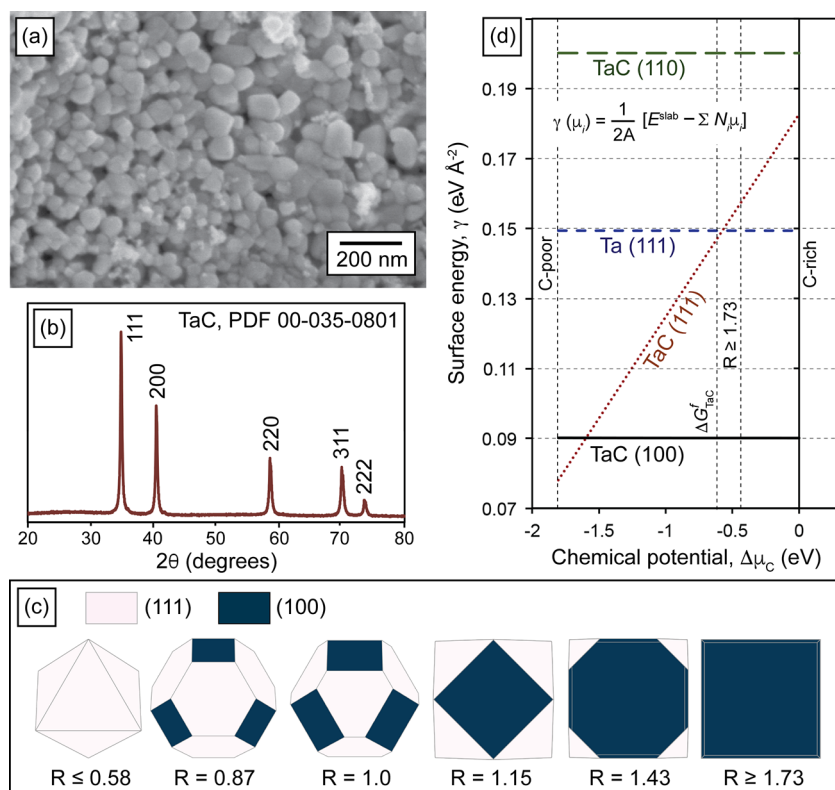


Figure 1. Characterization of undoped TaC powders, particle shapes, and surface energies. (a) Scanning electron micrograph and (b) X-ray diffraction pattern of undoped TaC powders. (c) Varying morphologies corresponding to the surface energy ratio ($R = \gamma_{111}/\gamma_{100}$) and (d) surface energies for the TaC(100), (111), and (110) slabs and the face-centered cubic Ta(111) slab as a function of the chemical potential of carbon ($\Delta\mu_C$).

$$\begin{aligned} \gamma(\Delta\mu_C, \Delta\mu_{\text{Ti}}, \Delta\mu_X) &= \frac{E^{\text{slab}+X} - \frac{N_{\text{Ta}}}{3} g_{\text{TiTa}_3\text{C}_4}^{\text{bulk}}}{2A} \\ &+ \Gamma_C(\Delta\mu_C + E_C^{\text{graphite}}) \\ &- \Gamma_{\text{Ti}}(\Delta\mu_{\text{Ti}} + E_{\text{Ti}}^{\text{hcp}}) \\ &- \Gamma_X(\Delta\mu_X + E_X^{\text{atom}}) \end{aligned} \quad (15)$$

In summary, we can generalize the surface energy of all systems as a linear equation with a constant value $\gamma(\Delta\mu_i = 0)$, which represents the surface energy when all chemical potential variables are set to 0 eV, as follows:

$$\gamma(\Delta\mu_i) = \gamma(\Delta\mu_i = 0) + \sum_i \Gamma_i \Delta\mu_i \quad (16)$$

All values of $\gamma(\Delta\mu_i = 0)$ and Γ_i for the surface energy of each slab are listed in Table 1.

RESULTS AND DISCUSSION

The morphologies of the undoped powders of TaC are illustrated in Figure 1a, showing that the nanoparticles are predominantly of random shapes, with minimal amounts of faceted surfaces. X-ray diffraction patterns of the powders can be observed in Figure 1b, where the lattice parameter obtained from Rietveld refinement is 4.4543 ± 0.00003 Å, indicating that the sample is slightly nonstoichiometric.^{44,45} Controlling the particle morphology requires tuning the relative growth rate of different crystal facets. Faster growth for a particular crystal face results in quicker extinction of that face, leaving the

slower growing faces as the enclosing surfaces for the final crystal. The growth rate of a particular face is directly proportional to its corresponding surface energy. Using the Wulff construction, Figure 1c illustrates how the equilibrium shape for a generic cubic material changes with the growth rate ratio ($R = \gamma_{111}/\gamma_{100}$). Values of R below 0.58 result in octahedrons, values between 0.58 and 1.73 result in cuboctahedrons, and values greater than 1.73 result in cubes. Burton et al.⁴⁶ previously proposed that facets with a high growth rate will go through thermodynamic roughening whereby the crystal morphology transitions from its equilibrium crystal shape to a round/irregular shape due to free energy minimization at elevated temperatures. More recently, Jin et al.²⁴ reported experimental thermodynamic roughening of transition metal carbides. In our case, it is likely that the growth rate of the $\{100\}$ facets has surpassed the temperature threshold for thermodynamic roughening due to the extremely high synthesis temperatures (>2000 K), thus explaining the lack of cubic particles and the lack of faceting in general in Figure 1a.

The surface energy with respect to the carbon chemical potential ($\Delta\mu_C$) is plotted in Figure 1d for undoped TaC surfaces (y -axis) for facets with Miller indices of (111), (110), and (100) and the (111) fcc Ta surface. For the stoichiometric slabs, such as (110) and (100), the surface energies are constant with respect to $\Delta\mu_C$. For the nonstoichiometric (111) Ta-terminated slab, however, the C-deficiency relative to the bulk TaC results in a positive linear relationship between γ_{111} and $\Delta\mu_C$ (see eq 2 and the Surface Grand Potential derivations). At high $\Delta\mu_C$, the most stable surface of TaC is

the (100) facet due to the smaller number of broken bonds compared to the (111) facet. At lower $\Delta\mu_C$, the Ta-terminated (111) facet is increasingly stabilized as it becomes more similar to the metallic fcc Ta (111) surface⁴⁷ with greater carbon deficiency. In fact, the calculated work function defined by

$$\Phi = V_{\text{vac}} - E_{\text{F}} \quad (17)$$

of the TaC(111) surface (4.62 eV) is close to that of the Ta(111) surface (4.70 eV), while that of the TaC(100) surface is significantly lower (3.61 eV). This stabilization of the (111) facet pushes its growth rate below that of roughening, allowing for minimal formation of cubooctahedrons but not the formation of cubes. In eq 17, V_{vac} is the calculated electrostatic potential in the vacuum of a slab, and E_{F} is the slab Fermi energy.

To expose crystal facets and tailor particle morphology, the surface energies of the desired facets must be further decreased. We add metallic dopants with low bulk solubility in TaC, namely Ni, Co, and Fe, as well as mixed Ni+Ti codopants, in order to modify its surface thermodynamics and subsequently influence its growth. A metallic dopant with high bulk solubility in TaC (i.e., Nb) was also added for comparison. The full list of prepared powders, with dopant concentrations determined by energy dispersive spectroscopy, is presented in Table 2. Figure 2 illustrates the morphology of

Table 2. Dopant Concentrations on the TaC Powders Determined from Energy Dispersive Spectroscopy^a

sample no. ^b	Ni (atom %)	Co (atom %)	Fe (atom %)	Nb (atom %)	Ni/Ti (atom %)
1	0.9	0.9	0.5	4.4	2.2
2	1.4	1.6	1.2	7.8	4.1
3	1.7	1.9	2.2	–	8.0
4	2.5	2.3	2.7	–	12.4
5	4.1	2.6	4.0	–	16.4
6	5.7	3.4	4.2	–	18.5
7	–	–	4.8	–	–

^aThe dopant concentrations listed for the Ni+Ti-doped TaC powders represent the concentrations of Ti in the powders. The concentration of Ni for these powders was fixed at 2.5 atom %. ^bIn the discussion, sample names are described using the dopant and sample number. For example, sample #1 with Ni doping is named Ni-1, sample #2 with Ni doping is named Ni-2, etc.

Fe-doped (Figure 2a), Ni+Ti-doped (Figure 2b), and Nb-doped (Figure 2c) TaC powders. The SEM micrographs show that significant numbers of the Fe-doped and Ni+Ti-codoped particles have been faceted into cubic particles (Figures 2a and b), whereas the Nb-doped powders have not (Figure 2c).

To compare the effectiveness in morphology control, we summarize the overall abundance of particles of different morphologies in Figure 3. As the abundance of nonfaceted particles decreases (Figure 3a) in order of undoped, Co-, Ni-, Fe-, and Ni+Ti co-doping, there is a corresponding increase in the abundance of faceted polyhedrons (Figure 3b) and cubic particles (Figure 3c). Cubic particles are only seen in the Fe-doped and Ni+Ti-doped powders in abundances of 38% and 42%, respectively. Thus, from the SEM images and the statistical analysis, we have established a causal relationship between the addition of certain dopants and the formation of morphologically controlled TaC particles.

In order to probe the effect of dopants on the surfaces, we compare the dopant concentrations of the morphology

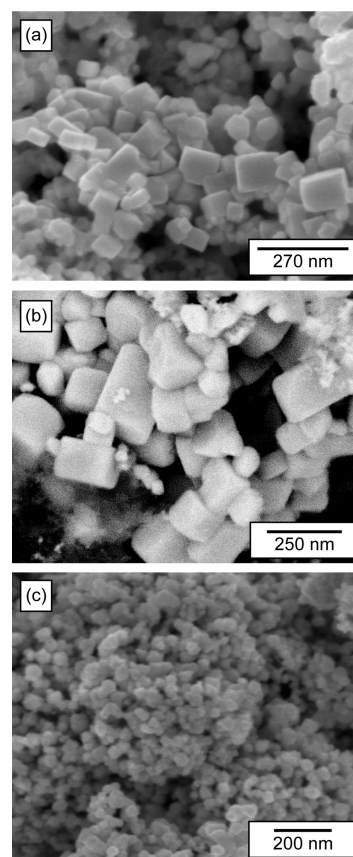


Figure 2. Electron microscopy of powders. Scanning electron micrographs for (a) Fe-doped, (b) Ni+Ti-doped, and (c) Nb-doped TaC powders.

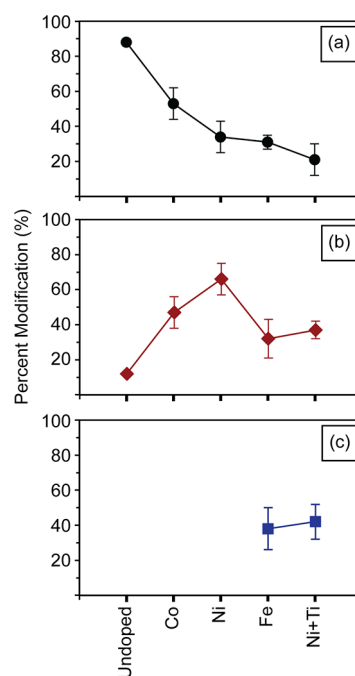


Figure 3. Statistical abundance of particle shapes. For the undoped, Co-, Ni-, Fe-, and Ni+Ti-doped TaC powders, the resulting morphologies are (a) nonfaceted, (b) faceted polyhedrons, and (c) cubic.

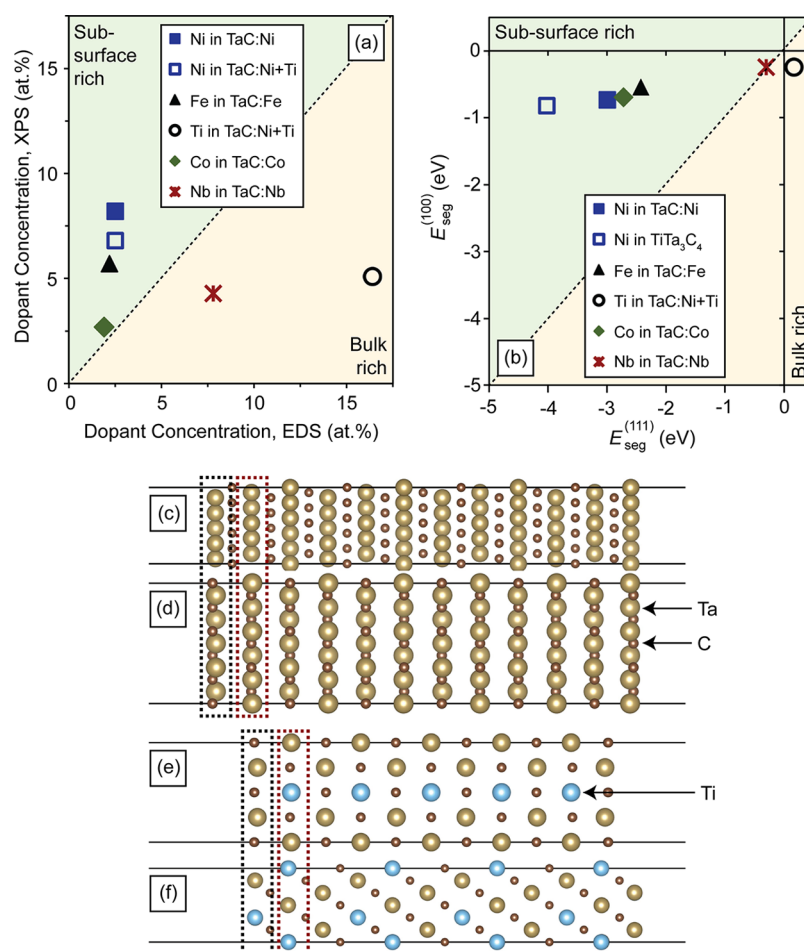


Figure 4. Dopant concentrations, surface energies, and slab models. (a) Plot of the concentration of dopants detected by X-ray photoelectron spectroscopy with respect to the concentration detected by energy dispersive spectroscopy. The samples chosen for comparison have the highest abundance of modified particles in each system, namely, Ni-4, Co-3, Fe-3, and NiTi-5 (see Table 2 for sample designations). (b) Calculated segregation energy for the (100) surface with respect to the (111) surface. Slab models for (c) TaC(111) and (d) TaC(100) used to calculate segregation energies in (b). Slab models for (e) TiTa_3C_4 (111) and (f) TiTa_3C_4 (100). The black (surface) and red (subsurface) dashed boxes indicate the possible metallic (i.e., Ta and/or Ti) sites a dopant can substitute. The slab models were constructed using lattice transformations to orient the basal plane parallel to the Miller index plane of interest. The oriented unit cell was then expanded along the direction normal to the basal plane followed by a removal of half the atoms in the resulting supercell to generate a slab and vacuum layer. The most stable termination for the (111) TaC surface is a Ta-terminated nonstoichiometric slab, while the (100) surface is modeled with a Ta–C-terminated stoichiometric slab.

modifiers (Co, Ni, Fe, and Ni+Ti) in the bulk using energy dispersive spectroscopy (penetration depth $\sim 1\text{--}2\ \mu\text{m}$ below the surface) and near the surface using X-ray photoelectron spectroscopy (penetration depth $< 10\ \text{nm}$ below the surface) in Figure 4a. The dopant with the greatest surface concentration enrichment (i.e., elemental concentration by XPS is greater than EDS) is Ni followed by Fe and Co. Ti and Nb have a high solubility in the bulk, as shown by the high EDS concentrations. Due to the chemical similarity of Ti and Ta, TiC is expected to be soluble in TaC leading to its high concentration in the bulk. Figure 4b illustrates the calculated surface segregation energies ($E_{\text{seg}}^{\text{surf}}$) for the TaC(111) and (100) facets for all dopants considered in the study. A negative $E_{\text{seg}}^{\text{surf}}$ indicates a driving force toward segregation to the surface, defined as the layer of atoms inside the black and red boxes in Figures 4c–f. In agreement with the experimental observations, Nb and Ti exhibit little to no preference to segregate to any surface because the segregation energies, illustrated in Figure 4b, show values close to zero for both $E_{\text{seg}}^{(111)}$ and $E_{\text{seg}}^{(100)}$. In contrast, Ni, Fe, and Co are predicted to strongly segregate to the (111) surfaces. In comparing the $E_{\text{seg}}^{(111)}$ and $E_{\text{seg}}^{(100)}$, it is clear

that the $E_{\text{seg}}^{(111)}$ values are less than $-2\ \text{eV}$, whereas $E_{\text{seg}}^{(100)}$ is closer to $-1\ \text{eV}$. To investigate how the high bulk solubility of Ti doping affects Ni doping for the case of the Ni+Ti-doped samples, we calculated $E_{\text{seg}}^{\text{surf}}$ for Ni in a TiTa_3C_4 solution and demonstrated that Ni will strongly segregate to the (111) surface. This is in qualitative agreement with the experimentally observed higher concentration of these dopants in the surface relative to the bulk.

To rationalize the relative preference of cuboctahedron/cube formation, enthalpy maps of R as a function of $\Delta\mu_{\text{C}}$ (y -axis) and $\Delta\mu_{\text{X}}$ (x -axis), where X is the dopant incorporated into TaC, are plotted in Figures 5a–c. Dopant segregation has two effects. First, the surface dopants modify the range of $\Delta\mu_{\text{C}}$ and $\Delta\mu_{\text{X}}$ where TaC is stable at the surface, as indicated by the red shaded regions. Second, the surface dopants also modify the surface energies of TaC and hence R , as a function of $\Delta\mu_{\text{C}}$ and $\Delta\mu_{\text{X}}$. In the case of Ni and Co doping (Figures 5a, b), the region where TaC is stabilized overlaps with those where cubes and/or cuboctahedrons will form. For Fe (Figure 5c), the region where TaC is stabilized overlaps with the region where cubes will form, making Fe a very efficient dopant. These

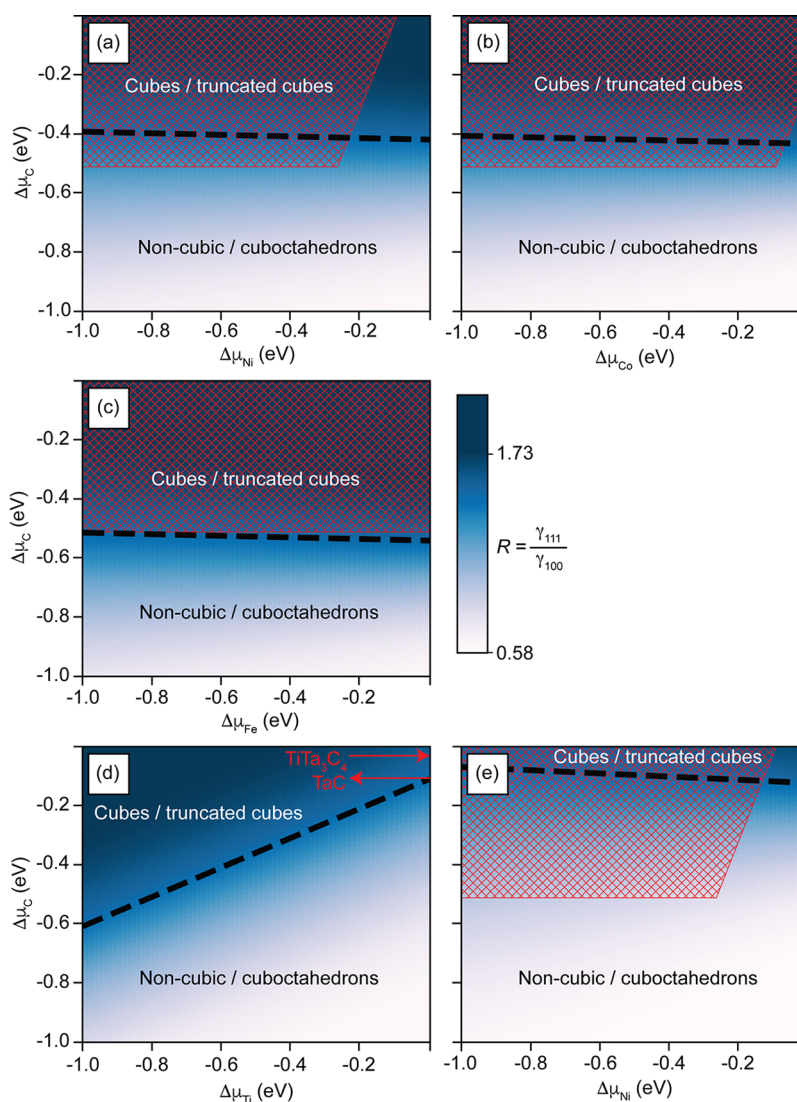


Figure 5. Calculated enthalpy maps of R as a function of $\Delta\mu_X$ with respect to $\Delta\mu_C$. (a) Ni in TaC, (b) Co in TaC, (c) Fe in TaC, (d) Ti in TiTa_3C_4 with $\Delta\mu_{\text{Ni}} = -0.4$ eV, and (e) Ni in TiTa_3C_4 with $\Delta\mu_{\text{Ti}} = -2$ eV at the surface. The dashed line indicates $R = 1.15$ (formation of cuboctahedrons) and partitions the enthalpy map into two regions. The region below is the $\Delta\mu$ window for the formation of (truncated) octahedrons, and the region above is the $\Delta\mu$ window for the formation of (truncated) cubes. The red shading indicates the section of the chemical potential map where TaC is stable. Red arrows in (d) indicate the chemical potential of $\Delta\mu_{\text{Ti}}$ where TiTa_3C_4 and TaC are stable.

observations explain the relative abundance of cubes observed under Fe doping and cuboctahedrons under Ni and Co doping in Figure 3.

Similarly, Figures 5d–e describe the enthalpy maps of R for Ni-doped TiTa_3C_4 , our computational analogue for Ni+Ti codoping. This analogue simulates Ni segregation on the surface of a TiTa_3C_4 slab in order to investigate the simultaneous effect of Ti doping in bulk solution and Ni doping on the surface of TaC. We stress that no TiTa_3C_4 was detected in the powders as a separate phase, and any interpretation of the computational analogue should not be used to imply the formation of this phase in the experimental work. Here, we kept a constant value of $\Delta\mu_{\text{Ni}} = -0.4$ eV for Figure 5d and $\Delta\mu_{\text{Ti}} = -2$ eV for Figure 5e, as these values are in the range of chemical potential where TaC is stable under $\Delta\mu_{\text{Ni}}$ with respect to $\Delta\mu_C$ and $\Delta\mu_{\text{Ti}}$ with respect to $\Delta\mu_C$, respectively. This leads to a larger chemical potential range that allows for the formation of cubes, in agreement with the statistical abundance of cubic versus faceted polyhedron particles shown

in Figure 3 for the Ni+Ti-doped powders. Since only dopants that segregate toward the surface will induce morphology modification, surface segregation is a prerequisite for influencing γ . This is further supported by the notion that Nb has little to no segregation preference toward the surface, which results in no signs of morphological modification (Figure 2c). We can therefore attribute the considerably lower percentage of faceted particles in the Co-doped system relative to the Ni-, Fe-, and Ni+Ti-doped systems to its comparatively low concentration on the surface (lower than ~ 3 atom %), as revealed by XPS.

We also calculated the negative integrated Crystal Orbital Hamiltonian Populations (–ICOHPs) for each dopant bond on the (100) and (111) surfaces^{41,42} to quantitatively gauge the contribution of covalent (dopant d and carbon p) and metallic (dopant d and Ta d) interactions to dopant bond strength (Figure 6a). We observe that for Fe doping in TaC, the majority of the contribution to dopant bond strength is from covalent (over 50%) interactions on the (100) surface

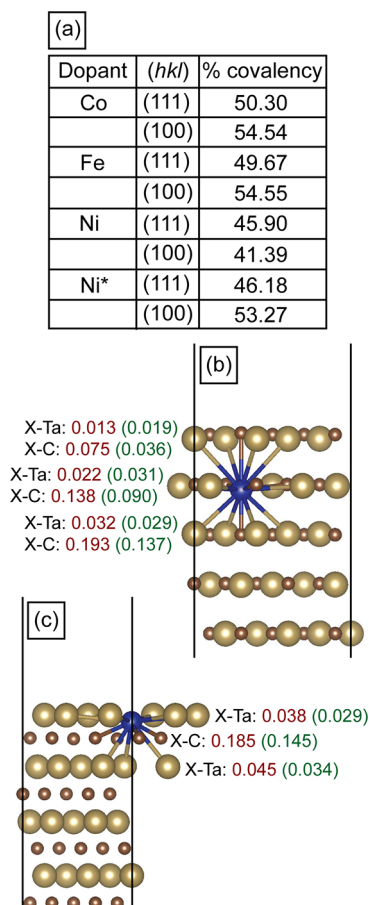


Figure 6. $-ICOHP$ bond contributions of dopant bonds at the surface. (a) Percentage of covalency for the dopant bonds at the surface and the corresponding metal atom that was substituted in the undoped surface. The remainder percentage represents metallicity. Ni* indicates Ni substituting Ti in $TiTa_3C_4$. The $-ICOHP$ contributions for all nearest X–Ta (metallic bonds) and X–C (covalent bonds) in the (b) (100) and (c) (111) surface are shown where X is the dopant (blue site). $-ICOHP$ values shown in red (green) text are for X = Fe (X = Ni).

and from metallic interactions on the (111) surface. Nie et al.²⁷ previously suggested that doping of Ni in TiC may lead to $p-d$ orbital hybridization between Ni and C at the (100) surface, which will further reduce its surface energy. In the case of Fe-doped TaC, we observe similar $p-d$ hybridization that stabilizes the (100) surface over the (111) surface, explaining the significantly higher yield of cubic nanoparticles. The significant decrease in γ up to $0.13 \text{ eV}\cdot\text{\AA}^{-2}$ when comparing the undoped surfaces to the Ni-, Fe-, and Co-doped surfaces at $\Delta\mu_i = 0 \text{ eV}$ will prevent the onset of thermodynamic roughening (see the last column of Table 1 for values of $\gamma(\Delta\mu_i = 0)$). When coupled with dopant and surface atom interactions, this decrease in surface energy is the root cause of the larger yield of faceted particles.

In summary, the onset of morphology modification is due to the surface segregation of dopants and interaction with neighboring carbon via $d-p$ hybridization, which reduces the growth rate to prevent thermodynamic roughening. Ni and Co doping favors faceted polyhedrons, while Fe doping favors both faceted polyhedrons and cubic geometries due to its stronger hybridization effect with neighboring C at the (100) surface. Nb segregates to the surface only minimally, and thus

faceted particles are not formed. Ti dopant dissolves in the bulk of the TaC host leading to a decrease in the surface chemical potential for Ti. This increases the chemical potential window that allows for cube formation. With the addition of Ni and carbon $p-d$ hybridization at the surface, thermodynamic roughening can be prevented, leading to cubic and faceted polyhedron geometries in the Ni+Ti-doped TaC.

CONCLUSIONS

We describe a systematic computation and experimental analysis of the surface energies and powder shapes in TaC doped with transition metals. Powders were prepared using a solvothermal synthesis approach, which permitted the straightforward incorporation of dopants such as nickel, iron, cobalt, niobium, and titanium. Dopant distribution within the powders was then determined using energy dispersive spectroscopy and X-ray photoelectron spectroscopy. The effectiveness of morphology control, from powders that show no special shapes to polyhedral and cubic powders, was found to depend on the dopant. Undoped and Nb-doped powders did not exhibit any shape control, whereas Co, Ni, Fe, and Ni+Ti resulted in an increasing abundance of faceted polyhedrons and cubic particles. Cubic particles, specifically, were seen in the Fe-doped and Ni+Ti-doped powders in abundances of 38% and 42%, respectively.

Density functional theory calculations were performed to predict surface energies and dopant segregation. We also calculated the negative integrated Crystal Orbital Hamiltonian Populations ($-ICOHPs$) for each dopant bond on the (100) and (111) surfaces to quantitatively determine the contribution of covalent (dopant d and carbon p) and metallic (dopant d and Ta d) interactions to dopant bond strength. The model predicted that the onset of morphology modification is due to surface segregation of dopants and interaction with neighboring carbon via $d-p$ hybridization. Ni and Co doping favors faceted polyhedrons, while Fe doping favors both faceted polyhedrons and cubic geometries due to its stronger hybridization effect with neighboring C at the (100) surface. Nb segregates to the surface only minimally, and thus faceted particles are not formed. Ti dissolves in the bulk of the TaC host leading to a decrease in the surface chemical potential for Ti. This increases the chemical potential window that allows for cube formation. The addition of Ni and carbon $p-d$ hybridization at the surface leads to cubic and faceted polyhedron geometries in the Ni+Ti-doped TaC. These results correlate with the experimental X-ray photoelectron and energy dispersive spectroscopy results, which show that the Co, Ni, and Fe segregate to the powder surfaces, whereas Nb and Ti do not.

We expect that the mechanisms explored here can be widely applicable to other combinations of dopants and ceramic powders. For example, if one seeks to produce highly faceted V-, Hf-, or Zr-carbide nanoparticles with fcc crystal structure, doping strategies reported here can be applied. Other rare earth elements may also be effective in changing the growth habits of crystals based on surface segregation and dopant-host atomic orbital hybridization.

AUTHOR INFORMATION

Corresponding Authors

Shyue Ping Ong – Department of NanoEngineering,
University of California San Diego, La Jolla, California

92093-0448, United States; orcid.org/0000-0001-5726-2587; Email: ongsp@eng.ucsd.edu

Olivia A. Graeve – Department of Mechanical and Aerospace Engineering, University of California San Diego, La Jolla, California 92093-0411, United States; orcid.org/0000-0003-3599-0502; Phone: +1 858 246-0146; Email: ograeve@ucsd.edu

Authors

Tianqi Ren – Department of Mechanical and Aerospace Engineering, University of California San Diego, La Jolla, California 92093-0411, United States

Richard Tran – Department of NanoEngineering, University of California San Diego, La Jolla, California 92093-0448, United States

Sebastian Lee – Department of Mechanical and Aerospace Engineering, University of California San Diego, La Jolla, California 92093-0411, United States

Aric Bandera – Department of Mechanical and Aerospace Engineering, University of California San Diego, La Jolla, California 92093-0411, United States

Manuel Herrera – Centro de Nanociencias y Nanotecnología, Universidad Nacional Autónoma de México, Ensenada, Baja California, C.P. 22800, México

Xiang-Guo Li – Department of NanoEngineering, University of California San Diego, La Jolla, California 92093-0448, United States

Complete contact information is available at:
<https://pubs.acs.org/10.1021/acs.jpcc.1c01387>

Author Contributions

[#]These authors contributed equally to this work.

Author Contributions

T.R., S.L., and A.B. conducted the syntheses of powders. T.R. performed diffraction and microscopy characterization of samples and analysis. R.T. carried out computational calculations and analysis. X.-G.L. provided guidance in computational calculations. M.H. performed XPS measurements and analysis. T.R. and R.T. wrote the initial manuscript. S.P.O. defined the computational modeling work. O.A.G. defined the experimental work and was the lead on the project. All authors contributed to and commented on the manuscript.

Notes

The authors declare no competing financial interest.

ACKNOWLEDGMENTS

The experimental work of this project was funded by grant W911NF-16-1-0585 from the Army Research Office to O.A.G. The support of the Frontier of Innovation Scholars Program graduate fellowship at the University of California San Diego to T.R. is gratefully acknowledged. R.T., X.G.L., and S.P.O. acknowledge the Materials Project, funded by the U.S. Department of Energy, Office of Science, Office of Basic Energy Sciences, Materials Sciences and Engineering Division under contract DE-AC02-05-CH11231: Materials Project program KC23MP, which supported the DFT computational studies performed in this work, as well as computational resources provided by the Triton Shared Computing Cluster (TSCC) at the University of California San Diego and the Extreme Science and Engineering Discovery Environment (XSEDE) supported by the National Science Foundation under grant ACI-1053575.

REFERENCES

- (1) Andrievskii, R. A.; Strel'nikova, N. S.; Poltoratskii, N. I.; Kharkhardin, E. D.; Smirnov, V. S. Melting point in systems ZrC-HfC, TaC-ZrC, TaC-HfC. *Powder Metall. Met. Ceram.* **1967**, *6*, 65–67.
- (2) Chen, H.; Liang, H.; Liu, L.; Li, H.; Liu, K.; Peng, F. Hardness measurements for high-pressure prepared TaB and nano-TaC ceramics. *Results Phys.* **2017**, *7*, 3859–3862.
- (3) Sani, E.; Mercatelli, L.; Fontani, D.; Sans, J.; Sciti, D. Hafnium and tantalum carbides for high temperature solar receivers. *J. Renewable Sustainable Energy* **2011**, *3*, 063107.
- (4) Desmaison-Brut, M.; Alexandre, N.; Desmaison, J. Comparison of the oxidation behaviour of two dense hot isostatically pressed tantalum carbide (TaC and Ta₂C) materials. *J. Eur. Ceram. Soc.* **1997**, *17*, 1325–1334.
- (5) Smith, C. J.; Ross, M. A.; De Leon, N.; Weinberger, C. R.; Thompson, G. B. Ultra-high temperature deformation in TaC and HfC. *J. Eur. Ceram. Soc.* **2018**, *38*, 5319–5332.
- (6) López, M.; Viñes, F.; Nolan, M.; Illas, F. Predicting the effect of dopants on CO₂ adsorption in transition metal carbides: case study on TiC (001). *J. Phys. Chem. C* **2020**, *124*, 15969–15976.
- (7) Chen, J. G. Carbide and nitride overlayers on early transition metal surfaces: preparation, characterization, and reactivities. *Chem. Rev.* **1996**, *96*, 1477–1498.
- (8) Yao, M.; Li, Q.; Hou, G.; Lu, C.; Cheng, B.; Wu, K.; Xu, G.; Yuan, F.; Ding, F.; Chen, Y. Dopant-controlled morphology evolution of WO₃ polyhedra synthesized by RF thermal plasma and their sensing properties. *ACS Appl. Mater. Interfaces* **2015**, *7*, 2856–2866.
- (9) Kaghazchi, P. Carbon-induced Ru nanorod formation. *RSC Adv.* **2014**, *4*, 1646–1649.
- (10) Tang, M. T.; Ulissi, Z. W.; Chan, K. Theoretical investigations of transition metal surface energies under lattice strain and CO environment. *J. Phys. Chem. C* **2018**, *122*, 14481–14487.
- (11) Qiao, S.; Novitskaya, E.; Ren, T.; Pena, G.; Graeve, O. A. Phase and morphology control of magnesium nanoparticles via lithium doping. *Cryst. Growth Des.* **2019**, *19*, 3626–3632.
- (12) Schmidt, K. M.; Mixture, S. T.; Graeve, O. A.; Vasquez, V. R. Metal hexaboride work functions: surface configurations and the electrical double layer from first-principles. *Adv. Electron. Mater.* **2019**, *5*, 1800074.
- (13) Schmidt, K. M.; Koch, R. J.; Mixture, S. T.; Graeve, O. A.; Vasquez, V. R. Phase stability analysis of ternary alkaline-earth hexaborides: insights from DFT calculations. *ACS Appl. Electron. Mater.* **2019**, *1*, 105–112.
- (14) Schmidt, K. M.; Mixture, S. T.; Graeve, O. A.; Vasquez, V. R. Interaction of hydrogen with MB₆ (M = Ba, Ca, La, and Sr) surfaces from first principles. *ACS Omega* **2019**, *4*, 65–72.
- (15) Schmidt, K. M.; Jaime, O.; Cahill, J. T.; Edwards, D.; Mixture, S. T.; Graeve, O. A.; Vasquez, V. R. Surface termination analysis of stoichiometric metal hexaborides: insights from first-principles and XPS measurements. *Acta Mater.* **2018**, *144*, 187–201.
- (16) Schmidt, K. M.; Buettner, A.; Graeve, O. A.; Vasquez, V. R. Interatomic pair potentials from DFT and molecular dynamics for Ca, Ba, and Sr hexaborides. *J. Mater. Chem. C* **2015**, *3*, 8649–8658.
- (17) Schmidt, K. M.; Graeve, O. A.; Vasquez, V. R. Ab initio and molecular dynamics-based pair potentials for lanthanum hexaboride. *J. Phys. Chem. C* **2015**, *119*, 14288–14296.
- (18) Kanakala, R.; Escudero, R.; Rojas-George, G.; Ramisetty, M.; Graeve, O. A. Mechanisms of combustion synthesis and magnetic response of high-surface-area hexaboride compounds. *ACS Appl. Mater. Interfaces* **2011**, *3*, 1093–1100.
- (19) Kanakala, R.; Rojas-George, G.; Graeve, O. A. Unique preparation of hexaboride nanocubes: a first example of boride formation by combustion synthesis. *J. Am. Ceram. Soc.* **2010**, *93*, 3136–3141.
- (20) Cahill, J. T.; Graeve, O. A. Hexaborides: a review of structure, synthesis and processing. *J. Mater. Res. Technol.* **2019**, *8*, 6321–6335.
- (21) Koch, R.; Metz, P. C.; Jaime, O.; Vargas-Consuelos, C. I.; Borja-Urby, R.; Ko, J. Y. P.; Cahill, J. T.; Edwards, D.; Vasquez, V. R.;

Graeve, O. A.; et al. Nanodomains and local structure in ternary alkaline-earth hexaborides. *J. Appl. Crystallogr.* **2018**, *51*, 1445–1454.

(22) Cahill, J. T.; Vasquez, V. R.; Misture, S. T.; Edwards, D.; Graeve, O. A. Effect of current on diffusivity in metal hexaborides: a spark plasma sintering study. *ACS Appl. Mater. Interfaces* **2017**, *9*, 37357–37363.

(23) Cahill, J. T.; Alberga, M.; Bahena, J.; Pisano, C.; Borja-Urby, R.; Vasquez, V. R.; Edwards, D.; Misture, S. T.; Graeve, O. A. Phase stability of mixed-cation alkaline-earth hexaborides. *Cryst. Growth Des.* **2017**, *17*, 3450–3461.

(24) Jin, S.; Shen, P.; Zhou, D.; Jiang, Q. A common regularity of stoichiometry-induced morphology evolution of transition metal carbides, nitrides, and diborides during self-propagating high-temperature synthesis. *Cryst. Growth Des.* **2012**, *12*, 2814–2824.

(25) Grove, D. E.; Gupta, U.; Castleman, A. W. Effect of carbon concentration on changing the morphology of titanium carbide nanoparticles from cubic to cuboctahedron. *ACS Nano* **2010**, *4*, 49–54.

(26) Grove, D. E.; Gupta, U.; Castleman, A. W. Effect of hydrocarbons on the morphology of synthesized niobium carbide nanoparticles. *Langmuir* **2010**, *26*, 16517–16521.

(27) Nie, J.; Wu, Y.; Li, P.; Li, H.; Liu, X. Morphological evolution of TiC from octahedron to cube induced by elemental nickel. *CrystEngComm* **2012**, *14*, 2213–2221.

(28) Kelly, J. P.; Graeve, O. A. Statistical experimental design approach for the solvothermal synthesis of nanostructured tantalum carbide powders. *J. Am. Ceram. Soc.* **2011**, *94*, 1706–1715.

(29) Kelly, J. P.; Kanakala, R.; Graeve, O. A. A solvothermal approach for the preparation of nanostructured carbide and boride ultra-high-temperature ceramics. *J. Am. Ceram. Soc.* **2010**, *93*, 3035–3038.

(30) Kresse, G.; Furthmüller, J. Efficient iterative schemes for ab initio total-energy calculations using a plane-wave basis set. *Phys. Rev. B: Condens. Matter Mater. Phys.* **1996**, *54*, 11169–11186.

(31) Kohn, W.; Sham, L. J. Self-consistent equations including exchange and correlation effects. *Phys. Rev.* **1965**, *140*, A1133–1138.

(32) Hacene, M.; Anciaux-Sedrakian, A.; Rozanska, X.; Klahr, D.; Guignon, T.; Fleurat-Lessard, P. Accelerating VASP electronic structure calculations using graphic processing units. *J. Comput. Chem.* **2012**, *33*, 2581–2589.

(33) Blöchl, P. E. Projector augmented-wave method. *Phys. Rev. B: Condens. Matter Mater. Phys.* **1994**, *50*, 17953–17979.

(34) Jain, A.; Ong, S. P.; Hautier, G.; Chen, W.; Richards, W. D.; Dacek, S.; Cholia, S.; Gunter, D.; Skinner, D.; Ceder, G.; et al. Commentary: the materials project: a materials genome approach to accelerating materials innovation. *APL Mater.* **2013**, *1*, 011002.

(35) Perdew, J. P.; Burke, K.; Ernzerhof, M. Generalized gradient approximation made simple. *Phys. Rev. Lett.* **1996**, *77*, 3865–3868.

(36) Sun, W.; Ceder, G. Efficient creation and convergence of surface slabs. *Surf. Sci.* **2013**, *617*, 53–59.

(37) Valvoda, V. X-ray diffraction study of Debye temperature and charge distribution in tantalum monocarbide. *Phys. Status Solidi A* **1981**, *64*, 133–142.

(38) Tran, R.; Xu, Z.; Radhakrishnan, B.; Winston, D.; Sun, W.; Persson, K. A.; Ong, S. P. Data descriptor: surface energies of elemental crystals. *Sci. Data* **2016**, *3*, 160080.

(39) Tasker, P. W. The stability of ionic crystal surfaces. *J. Phys. C: Solid State Phys.* **1979**, *12*, 4977–4984.

(40) Ong, S. P.; Richards, W. D.; Jain, A.; Hautier, G.; Kocher, M.; Cholia, S.; Gunter, D.; Chevrier, V. L.; Persson, K. A.; Ceder, G. Python materials genomics (pymatgen): a robust, open-source python library for materials analysis. *Comput. Mater. Sci.* **2013**, *68*, 314–319.

(41) Maintz, S.; Deringer, V. L.; Tchougréeff, A. L.; Dronskowski, R. LOBSTER: a tool to extract chemical bonding from plane-wave based DFT. *J. Comput. Chem.* **2016**, *37*, 1030–1035.

(42) Sun, W.; Bartel, C. J.; Arca, E.; Bauers, S. R.; Matthews, B.; Orvañanos, B.; Chen, B.; Toney, M. F.; Schelhas, L. T.; Tumas, W.; et al. A map of the inorganic ternary metal nitrides. *Nat. Mater.* **2019**, *18*, 732–739.

(43) Stull, D. R.; Prophet, H. *JANAF Thermochemical Tables*, 2nd ed.; U.S. National Bureau of Standards: Washington, DC, 1971.

(44) Bowman, A. L. The variation of lattice parameter with carbon content of tantalum carbide. *J. Phys. Chem.* **1961**, *65*, 1596–1598.

(45) Kelly, J. P.; Graeve, O. A. Mechanisms of pore formation in high-temperature carbides: case study of TaC prepared by spark plasma sintering. *Acta Mater.* **2015**, *84*, 472–483.

(46) Burton, W. K.; Cabrera, N.; Frank, F. C. The growth of crystals and the equilibrium structure of their surfaces. *Philos. Trans. R. Soc. London, Ser. A* **1951**, *243*, 299–358.

(47) Zaima, S.; Shibata, Y.; Adachi, H.; Oshima, C.; Otani, S.; Aono, M.; Ishizawa, Y. Atomic chemical composition and reactivity of the TiC(111) surface. *Surf. Sci.* **1985**, *157*, 380–392.